The facile fabrication of 2D/3D Z-scheme g-C$_3$N$_4$/UiO-66 heterojunction with enhanced photocatalytic Cr(VI) reduction performance under white light

Xiao-Hong Yi, Si-Qi Ma, Xue-Dong Du, Chen Zhao, Huifen Fu, Peng Wang, Chong-Chen Wang*

Beijing Key Laboratory of Functional Materials for Building Structure and Environment Remediation/Beijing Advanced Innovation Centre for Future Urban Design, Beijing University of Civil Engineering and Architecture, Beijing 100044, PR China

HIGHLIGHTS

- The g-C$_3$N$_4$/UiO-66 (BGxUy) composites were facilely prepared by ball-milling.
- The BGxUy achieved robust photocatalytic Cr(VI) reduction under white light.
- The Z-scheme mechanism of Cr(VI) reduction over BG60U40 is proposed and affirmed.

GRAPHICAL ABSTRACT
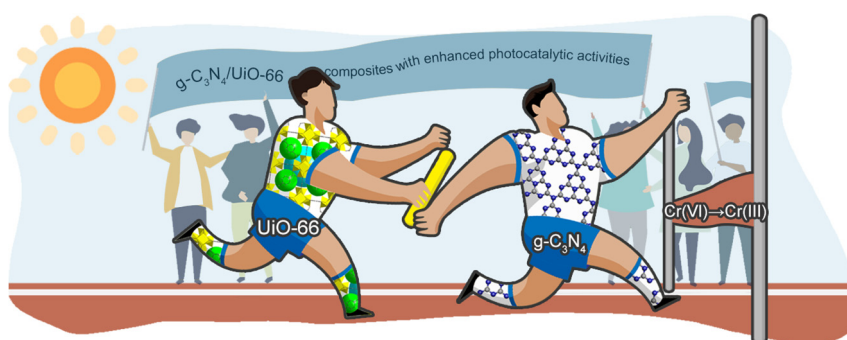
ARTICLE INFO

ABSTRACT

Z-scheme g-C$_3$N$_4$/UiO-66 (BGxUy) heterojunctions constructed from 3D UiO-66 and 2D g-C$_3$N$_4$ sheets were facilely fabricated using ball-milling method, which were characterized by scanning electron microscopy (SEM), transmission electron microscopy (TEM), high-resolution transmission electron microscopy (HRTEM), powder X-ray diffraction (PXRD), Fourier transform infrared spectroscopy (FTIR), X-ray photoelectron spectroscopy (XPS), N$_2$ adsorption-desorption measurement (BET), thermogravimetric analysis (TGA), UV–Vis diffuse reflectance spectroscopy (UV–Vis DRS), photoluminescence spectroscopy (PL), electrochemical impedance spectroscopy (EIS), electron spin resonance (ESR) and density functional theory (DFT) calculations. The photocatalytic activities of Cr(VI) reduction over the BGxUy heterojunctions were tested upon the irradiation of white light. The influence factors on photocatalytic performances of BG60U40 like different organics, pH and different co-existing foreign ions (ions in lake water, tap water, simulated sea water, and simulated leather tanning water) were clarified. The experiment results demonstrated that the optimal BG60U40 exhibited superior Cr(VI) reduction efficiency than pristine UiO-66 and g-C$_3$N$_4$ due to the declined recombination of photo-induced charge carriers. As well, the heterojunction displayed good reusability and stability in the cyclic experiment. The corresponding Z-scheme mechanism of photocatalytic Cr(VI) reduction was proposed and verified by electrochemical analysis, ESR measurement and DFT calculations.

1. Introduction

UiO-66, as a typical metal–organic framework (MOF), attracted wide attention due to its ultrahigh surface area along with ultrahigh thermal/chemical stability [1–5]. Up to now, it had been applied in wide research areas like catalysis [6,7], gas adsorption/separation [8–12], photocatalysis [12–18], adsorptive removal of pollutants from wastewater [19]. UiO-66′s photocatalytic activity was firstly tapped to produce H_2 gas upon the irradiation of ultraviolet lamp ($\lambda = 300$ nm). However, UiO-66 exhibited the limited photocatalytic performances, which could be attributed to their declining photo-induced electron-hole charge separation and limited light utilization ability [12–17,20,21]. To overcome the above-stated drawbacks of UiO-66, the metal-free graphite-like C_3N_4 (g-C_3N_4) was selected to construct binary g-C_3N_4/UiO-66 heterojunction composites [22,23]. Yuan and co-workers constructed the g-C_3N_4/UiO-66 quasi-polymeric composites via annealing to accomplish enhanced H_2 production under the visible light [24]. Liu and co-workers prepared g-C_3N_4/UiO-66 nanohybrids by in-situ solvothermal method to decompose rhodamine B (RhB) upon the visible light illumination [25]. Zhou and coworkers fabricated g-C_3N_4/UiO-66 heterojunction using facile annealing method, which was used to decompose methylene blue (MB) efficiently under visible light [26]. Ye and coworkers fabricated g-C_3N_4/UiO-66 hybrids via electrostatic self-assembly method to carry out CO_2 transformation under the visible light [27]. To our best knowledge, up to now no study on photocatalytic Cr(VI) reduction over Z-scheme g-C_3N_4/UiO-66 heterojunction was reported.

Hexavalent chromium usually exists in wastewater from chromate manufacturing, electroplating, paint-making, leather tanning and other industries [28–31]. Hexavalent chromium is easily adsorbed by human body, and it can exert potential threat to human health through digestion, respiratory tract, skin and mucosa [30]. When Cr(VI) is reduced to Cr(III), the toxicity of chromium can be greatly reduced [28,32]. Therefore, it is of great significance to eliminate Cr(VI) from wastewater. In recent years, more and more attentions concerning Cr(VI) photoreduction into Cr(III) have been paid to its application in wastewater treatment [22,33], which is easily to be removed as precipitated solid wastes like $Cr(OH)_3$ [30].

Within this paper, series two-dimensional/three-dimensional (2D/3D) g-C_3N_4/UiO-66 composites were facilely prepared via ball-milling method (Scheme 1), which were characterized and used as white light - responsive photocatalysts to achieve outstanding reduction of hexavalent chromium under lower pH conditions.

2. Experimental

The used chemicals, the characterization instruments, and DFT computation details were listed in electronic Supplementary Information (ESI).
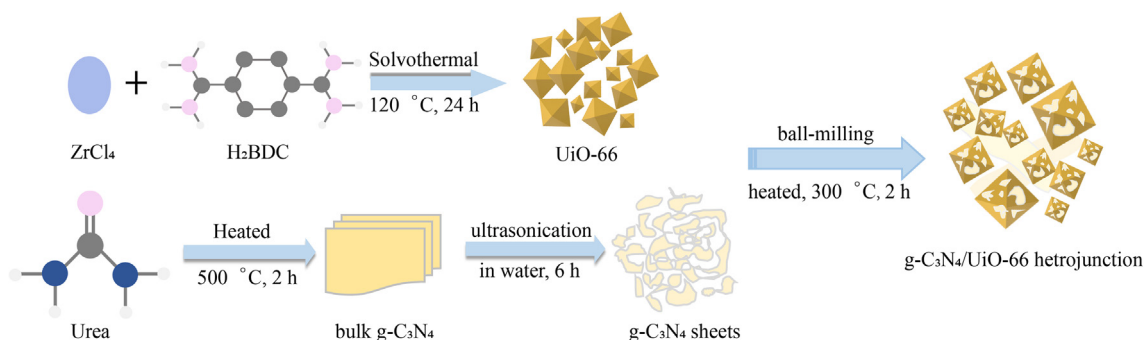
2.1. Preparation of g-C_3N_4/UiO-66 composites

The g-C_3N_4 was prepared by pyrolysis of urea without any template [34]. Briefly, a certain quantity of urea pellets (10.0 g in this study) were placed in a crucible with cover and were heated up to 500 °C for 120 min using a muffle furnace. The obtained bulk g-C_3N_4 were ultrasonically exfoliated in deionized (DI) water for 6 h, and the g-C_3N_4 sheets were separated by centrifugation (yield 4.0% based on urea).

UiO-66 octahedrons were solvothermally synthesized following the procedure reported in previous report [24]. The solutions of 40.0 mg $ZrCl_4$ and 28.5 mg H_2bdc (benzene-1,4-dicarboxylic acid) dissolved in 5.0 mL DMF (N,N-dimethylformamide) were mixed completely, in which 3.0 mL acetic acid was added to regulate the UiO-66′s morphology. The matrix was transferred into a 25.0 mL teflon-lined bomb, followed by being heated at 120 °C for 24 h. Finally, the UiO-66 samples were obtained via centrifugation after cooling to ambient temperature.

The g-C_3N_4 and UiO-66 samples were mixed with the aid of ball-milling (30 Hz, 20 min). The obtained matrix was heated with an increase rate of 5 °C min^{-1} and maintained at 300 °C for 120 min under the N_2 atmosphere in a tube furnace. The composites with the various mass ratios of g-C_3N_4/UiO-66 were obtained, referred as BG*x*U*y* (the letters "B", "G" and "U" are abbreviated for ball milling, g-C_3N_4, and UiO-66. The variables "*x*" and "*y*" are the percentage of g-C_3N_4 and UiO-66 in the total mass of composites, respectively).
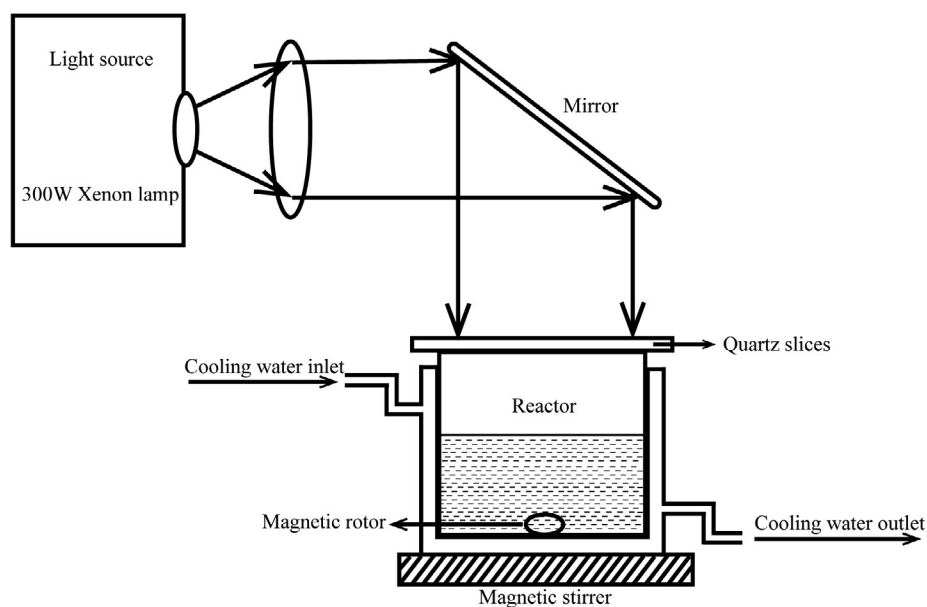
2.2. Photocatalytic activity

The 200.0 mL $K_2Cr_2O_7$ aqueous solution with initial concentration of 10.0 mg L^{-1} (based on Cr(VI)) was selected to evaluate the photocatalytic properties of heterojunctions with the photocatalyst dosage of 500.0 mg L^{-1} under white light provided by a Xe light with the power of 300 W (Beijing Aulight Co., Ltd). After the adsorption–desorption equilibrium was accomplished within 60 min in the dark condition, the targeted solution was irradiated by 300 W white light. During illumination, 1.5 mL solution was extracted from the reactor every 20 min for subsequent determination. The residual Cr(VI) content in the filtrate was measured with the 1,5-diphenylcarbazide method [35] on a Laspec Alpha-1860 spectrometer. The schematic illustration of the experimental set-up for photocatalytic reaction and the white light spectrum were depicted in Scheme 2 and Fig. S1, respectively.

3. Results and discussion

3.1. Characterizations

The PXRD patterns of g-C_3N_4, UiO-66, and series UiO-66/g-C_3N_4 (BG*x*U*y*) composites were depicted in Fig. 1a. It was quite obvious that the PXRD patterns of UiO-66 were in good agreement with the simulated ones from single crystal structure data [36] and related references [37]. As well, the PXRD patterns of obtained g-C_3N_4 were well-matched with the standard one (JCPDS No. 87-1526), in which the characteristic

Scheme 1. Diagrammatic sketch of the g-C_3N_4/UiO-66 composites fabricated via ball-milling and thermal treatment.

Scheme 2. Schematic diagram of the experimental device for photocatalytic reaction.

diffraction peak at 27.4° was attributed to (0 0 2) planes of g-C$_3$N$_4$ sheets and the typical inter-plane stacking graphitic layered structure [38,39]. In the PXRD patterns of UiO-66/g-C$_3$N$_4$ (BGxUy, especially for BG90U10, BG80U20 and BG70U30 with low UiO-66 content) composites, the characteristic PXRD peaks of both g-C$_3$N$_4$ and UiO-66 could be observed clearly, and no additional peaks of crystalline impurities could be observed, indicating that the original structures of g-C$_3$N$_4$ and UiO-66 were maintained well, and no crystalline impurities were produced during the ball-milling process. It was remarkable that the characteristic peak at 27.4° of g-C$_3$N$_4$ became more obvious with the increasing g-C$_3$N$_4$ content. The unaltered backbone structures of g-C$_3$N$_4$ and UiO-66 in BGxUy composites were confirmed by FTIR (Fig. 1b). The peak located at 810 cm^{-1} can be assigned to the characteristic tri-s-triazine rings in g-C$_3$N$_4$, while the intense peaks located between the 1200–1650 cm^{-1} could be attributed to the C-N rings with stretching modes in g-C$_3$N$_4$ [40,41]. As well, with the increased percentage of UiO-66 in the hybrids, the absorption peaks ranging from 600 cm^{-1} to 800 cm^{-1} could be observed more clearly, which were associated to Zr-O$_2$ in both longitudinal and transverse modes [42,43].

The formation of electronic interactions is crucial to achieve the efficient interfacial charge transfer between g-C$_3$N$_4$ and UiO-66 [44]. Therefore, XPS was carried out to investigate the interaction between g-C$_3$N$_4$ and UiO-66 in UiO-66/g-C$_3$N$_4$ composite. As depicted in Fig. 2a,

the XPS determination displayed that the two obvious N 1s and Zr 3d peaks could be attributed to the g-C$_3$N$_4$ and UiO-66, respectively. The peaks with binding energies of 400.43, 398.84 and 398.14 eV could be ascribed to the characteristic N-(C)$_3$, pyridinic N, and C-N=C bond of g-C$_3$N$_4$, respectively (Fig. 2b) [45–47]. After the combination of g-C$_3$N$_4$ and UiO-66 (like BG60U40), it was obviously to find that the binding energies of N 1s belonging to N-(C)$_3$, pyridinic N, and C-N=C bond were shifted from 400.43, 398.84 and 398.14 eV in g-C$_3$N$_4$ to 400.1, 398.57 and 398.1 eV in BG60U40 [48–50]. It could be attributed to the redistribution of additional electrons in BG60U40 system, and the shift of N 1s peaks in g-C$_3$N$_4$ towards the low binding energy direction further confirmed the electron transfer from UiO-66 to g-C$_3$N$_4$ after their coupling [51].

The smooth octahedral of pristine UiO-66 with particle size ranging from 500 to 1000 nm (Figs. 3a and 4a) and the g-C$_3$N$_4$ sheets (Figs. 3b and 4b) can be observed via SEM and TEM. After ball-milling treatment, it can be found that the g-C$_3$N$_4$ sheets were wrapped onto the surface of octahedral UiO-66 to fabricate rough UiO-66/g-C$_3$N$_4$ composite (like BG60U40) without any destroy toward the structures of UiO-66 and g-C$_3$N$_4$ (Figs. 3c, d, 4c and d). To elucidate the microscopic structure and element content of the BG60U40 composites, a more detailed investigation was conducted using HRTEM and SEM-EDS. Obviously, the g-C$_3$N$_4$ sheets are wrapped onto UiO-66 (Fig. 5), which is further
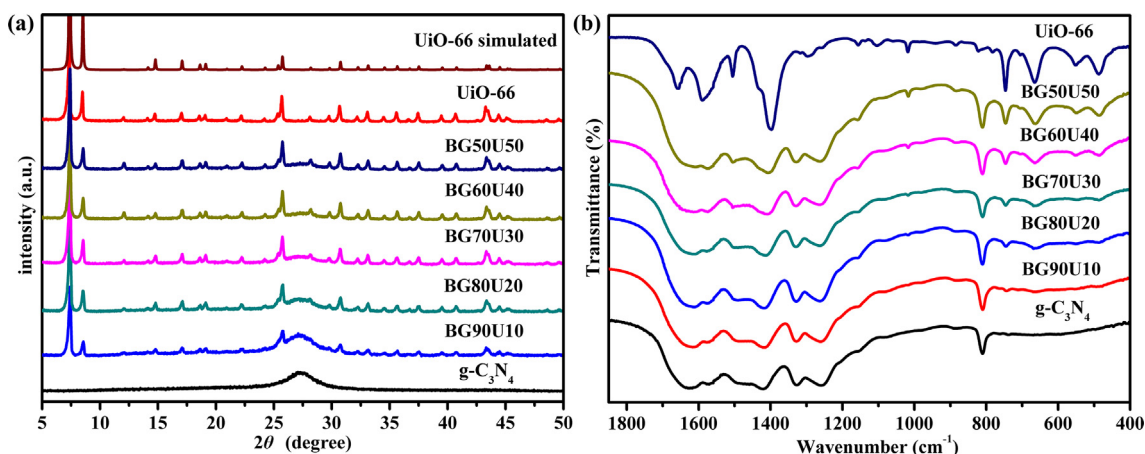

Fig. 1. (a) The XRD patterns and (b) the FTIR spectra of the pristine g-C$_3$N$_4$, UiO-66 and series composites.
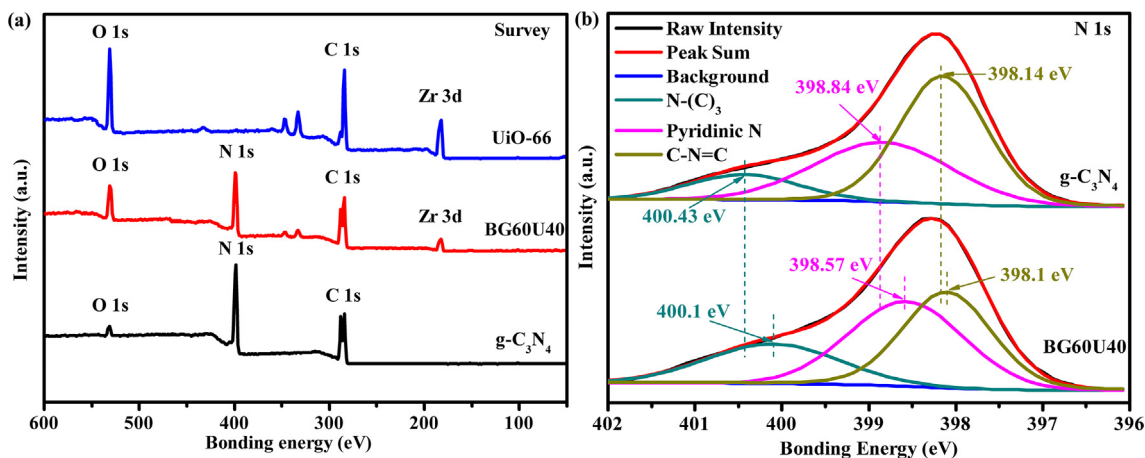
Fig. 2. The XPS spectra of pristine g-C$_3$N$_4$, UiO-66 and BG60U40: (a) survey scan, (b) N 1s.

confirmed by the distribution of O, Zr (the characteristic element from UiO-66) and N (the characteristic element from g-C$_3$N$_4$) throughout the BG60U40 composite (Fig. 6). All the above-stated characterizations indicated the successful construction of g-C$_3$N$_4$/UiO-66 (BGxUy) composites. It was more facile to construct the g-C$_3$N$_4$/UiO-66 (BGxUy) composites via ball-milling than annealing [24,26], electrostatic reaction [27] and in-situ solvothermal method [25].

The UV–Vis DRS was recorded to characterize the optical absorption property of all g-C$_3$N$_4$/UiO-66 heterojunctions. The E_g value (band gap energy) was calculated according to the Eq. (1) [52].

$$\alpha h\upsilon = A(h\upsilon - E_g)^{n/2} \tag{1}$$

where α, h and υ are the diffuse absorption coefficient, the light constant, and the frequency, respectively. n is judged by the optical transition type of the semiconductor (indirect ($n = 4$) or direct ($n = 1$)). In this study, n is assigned as 4 because BG60U40 is indirect semiconductor, which matches well with the previous reports [53,54].

As depicted in Fig. 7a and 7b, UiO-66 and g-C$_3$N$_4$ displayed absorption edges at 320 nm with E_g being ca. 3.88 eV and 443 nm with E_g being 2.80 eV, respectively. In contrast, the absorption edge of BGxUy exhibited obvious red shift to ca. 446 nm with E_g being ca 2.78 eV,

implying that BGxUy composites could be excited by the visible light with longer wavelength. The similar findings are observed in the g-C$_3$N$_4$/UiO-66 composite prepared via electrostatic reaction (2.78 eV) [27]. However, the E_g of the as-prepared BG60U40 in our work was narrower than those of counterpart composites prepared via in-situ hydrothermal method (3.79 eV) [25] and annealing treatment (2.92 eV) [26], indicating that ball-milling followed by thermal treatment facilitates the construction of heterojunction responsive to visible light. And, it was observed that the visible light responsive g-C$_3$N$_4$ dominates the optical properties of the BGxUy composites, which may be due to the interface formed between g-C$_3$N$_4$ and UiO-66.

The Mott-Schottky plots of the pristine g-C$_3$N$_4$ and UiO-66 were measured at different frequencies to estimate the flat band potential as shown in Fig. 7c and 7d. And the positive relationship of the obtained C^{-2} to the potential confirmed that they are typical n-type semiconductors [55]. The conduction band (CB) of the pristine g-C$_3$N$_4$ and UiO-66 were determined to be ca. −1.11 eV and −0.75 eV ($E_{CB} = E_{VB} - E_g$) [56] *versus* the Ag/AgCl electrode at pH = 7, respectively.

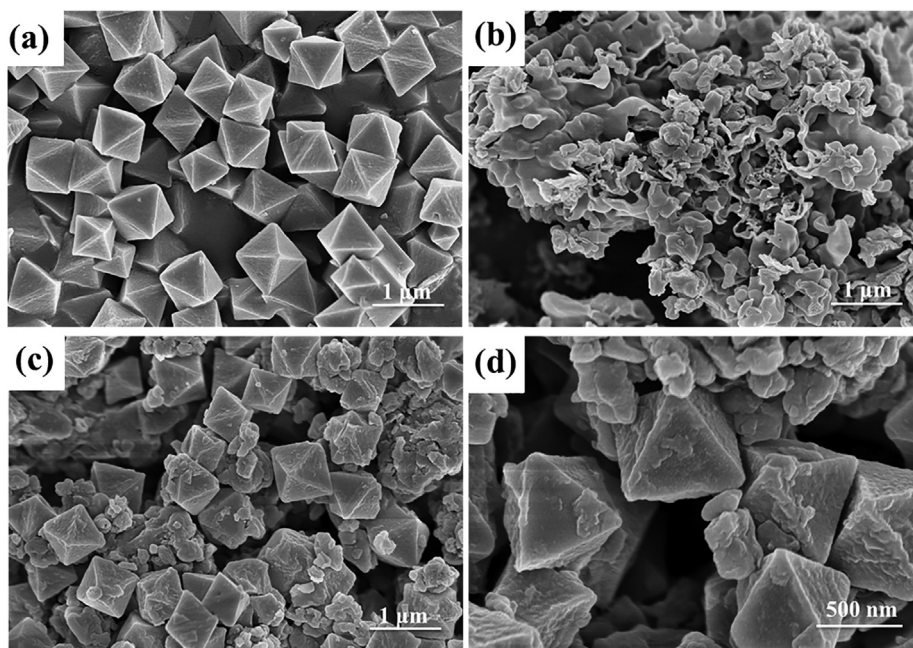**Fig. 3.** The SEM images of (a) pristine UiO-66, (b) pristine g-C$_3$N$_4$, (c) and (d) BG60U40 composite.
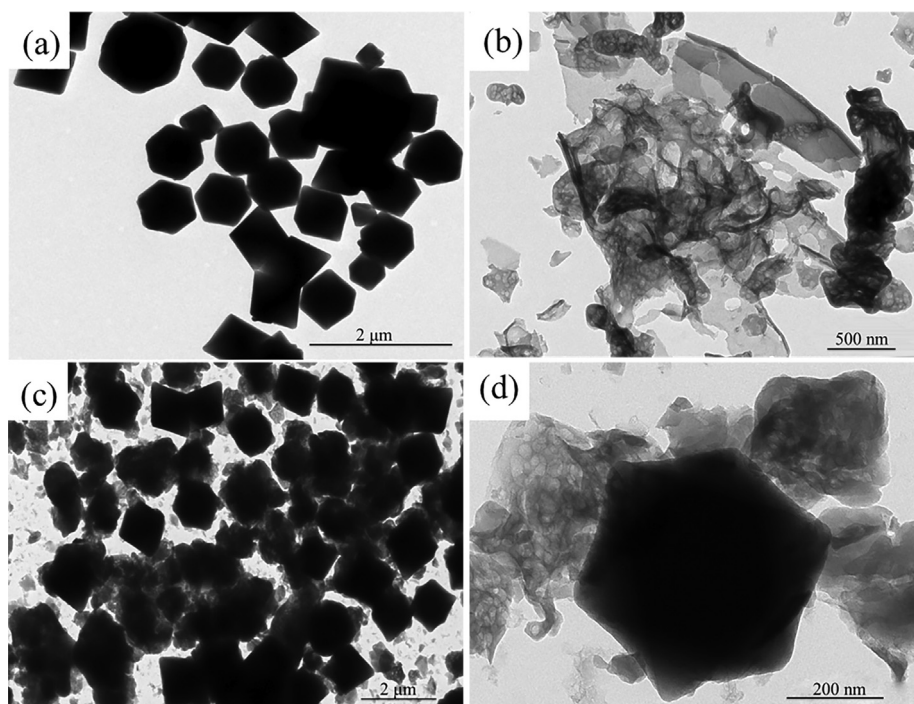
Fig. 4. The TEM images of (a) pristine UiO-66, (b) pristine g-C₃N₄, (c) and (d) BG60U40 composite.

3.2. Photocatalytic performances

3.2.1. Photocatalytic Cr(VI) reduction

The photocatalytic performances of Cr(VI) reduction over all the samples were studied under white light irradiation. Upon the irradiation of white light, all BGxUy composites displayed higher photocatalytic performances toward Cr(VI) reduction than those of pristine g-C₃N₄ and UiO-66, in which BG60U40 composite exhibited best Cr(VI) reduction activity with efficiency of 99% within 40 min (Fig. 8a). The kinetic plots of photocatalytic Cr(VI) reduction over
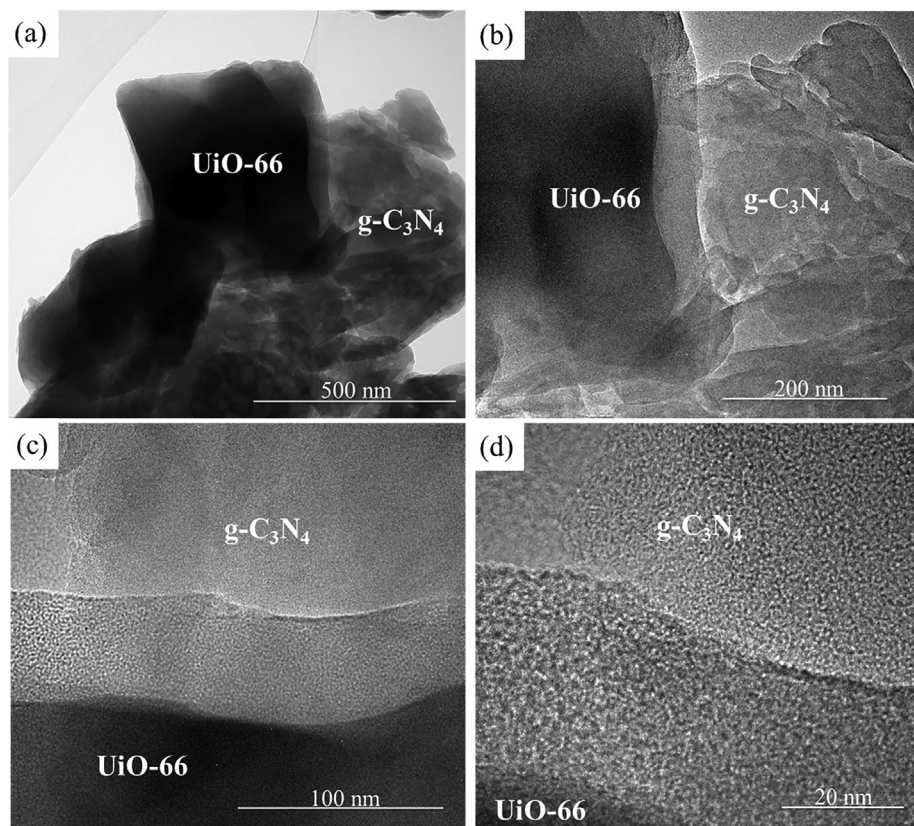

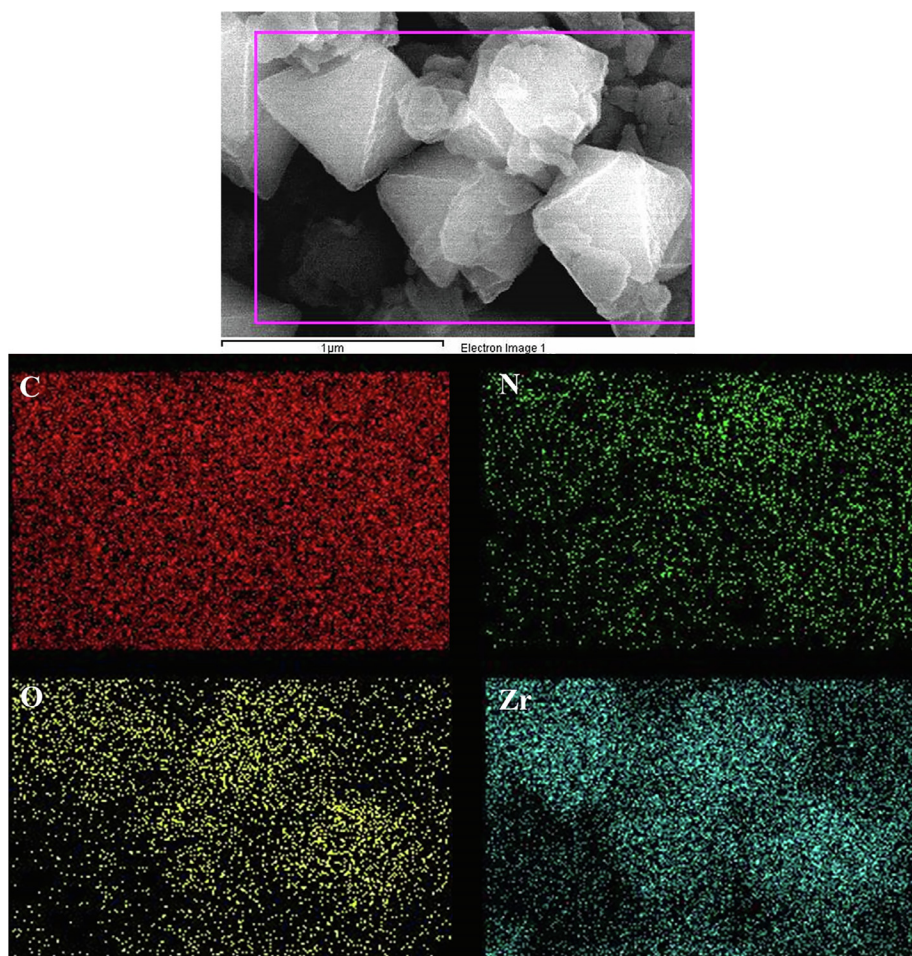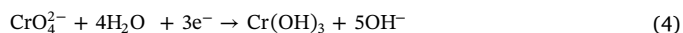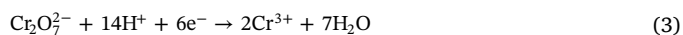**Fig. 5.** The HRTEM images of BG60U40 composite.

Fig. 6. The EDS elemental mappings of BG60U40 composite.

BGxUy composites were fitted to the pseudo-first order model ($\ln[C/C_0] = -kt$) [57], in which C_0, C and k are the initial Cr(VI) concentration, the residual Cr(VI) concentrations at different reaction times and reaction rate constant, respectively. The photocatalytic Cr(VI) reduction rates (k values) over the different photocatalysts followed the order of BG60U40 > BG70U30 > BG80U20 > g-C$_3$N$_4$/UiO-66 matrix > BG50U50 > BG90U10 > g-C$_3$N$_4$ > UiO-66 (Fig. 8b), which exhibited saddle-shaped curve with the introduced contents of g-C$_3$N$_4$ in BGxUy composites. It is noteworthy that the g-C$_3$N$_4$/UiO-66 matrix refers to the physical mixture of g-C$_3$N$_4$ (60 mg) and UiO-66 (40 mg) without further ball-milling and thermal treatment. Comparing with the counterpart photocatalysts previously reported, the BG60U40 composite also exhibited superior catalytic activity toward Cr(VI) reduction under the similar reaction conditions (Table 1). It was worthy to noting that the introduction of g-C$_3$N$_4$ onto UiO-66 led to the decreasing surface area from 1014.5 m^2 g^{-1} for pristine UiO-66 to 434 m^2 g^{-1} for BG60U40 and 100.1 m^2 g^{-1} for BG90U10 (Fig. S2 and Table S1). In the view of photocatalytic Cr(VI) reduction performances, the order of BG60U40 > BG70U30 > BG80U20 > BG90U10 matched well with the enhanced surface area, which were comparable to the other g-C$_3$N$_4$/MOF composites [23]. Generally, the increasing surface area can lead to the enhanced photocatalytic performance of the catalyst, as it can offer more active sites to boost the charge transfer over the composite interfaces along with the utilization of visible light [58]. However, excessive UiO-66 (like BG50U50) may deteriorate the quality of effective heterogeneous interface in BGxUy, which is not beneficial to charge transfer of the heterogeneous interface [59].

3.2.2. Effect of initial pH

It is worthy to noting that the photocatalytic reaction is generally heavily affected by the solution pH, considering that pH can influence both the acid-base condition of the reaction system and the existing species of the treated targets [34]. As illustrated in Fig. 9a and b, the photocatalytic Cr(VI) reduction efficiencies and the reaction rates (k values) [34] varied significantly under different pH conditions. The reduction efficiencies increased significantly with the decreasing pH (99.0%, 51.2%, 28.0%, 23.1%, 22.9%, 21.0% and 25.0% at pH being 2.0, 3.0, 4.0, 5.0, 6.0, 7.0 and 8.0, respectively). Under acidic environments, the Cr(VI) photoreduction over BG60U40 was achieved following Eq. (2) and (3) [65,66], in which the excessive H$^+$ was beneficial to the transformation from Cr(VI) to Cr(III) [30]. In contrast, under alkaline environment, Cr(VI) is mainly presented as CrO$_4^{2-}$ [67], and the corresponding Cr(VI) reduction was accomplished following Eq. (4) [34]. Moreover, the formed Cr(OH)$_3$ precipitates under high pH condition will mask the active sites of BG60U40 photocatalyst, resulting into the declining Cr(VI) reduction performance [30,68].

$$BGxUy + h\nu \rightarrow BGxUy(h^+ + e^-) \tag{2}$$

$$Cr_2O_7^{2-} + 14H^+ + 6e^- \rightarrow 2Cr^{3+} + 7H_2O \tag{3}$$

$$CrO_4^{2-} + 4H_2O + 3e^- \rightarrow Cr(OH)_3 + 5OH^- \tag{4}$$

3.2.3. Influence of different hole scavengers

Upon the irradiation of light with suitable wavelength, the photo-induced electron-hole pair will be produced. During the Cr(VI) reduction process, if the holes (h$^+$) were consumed, the separation of
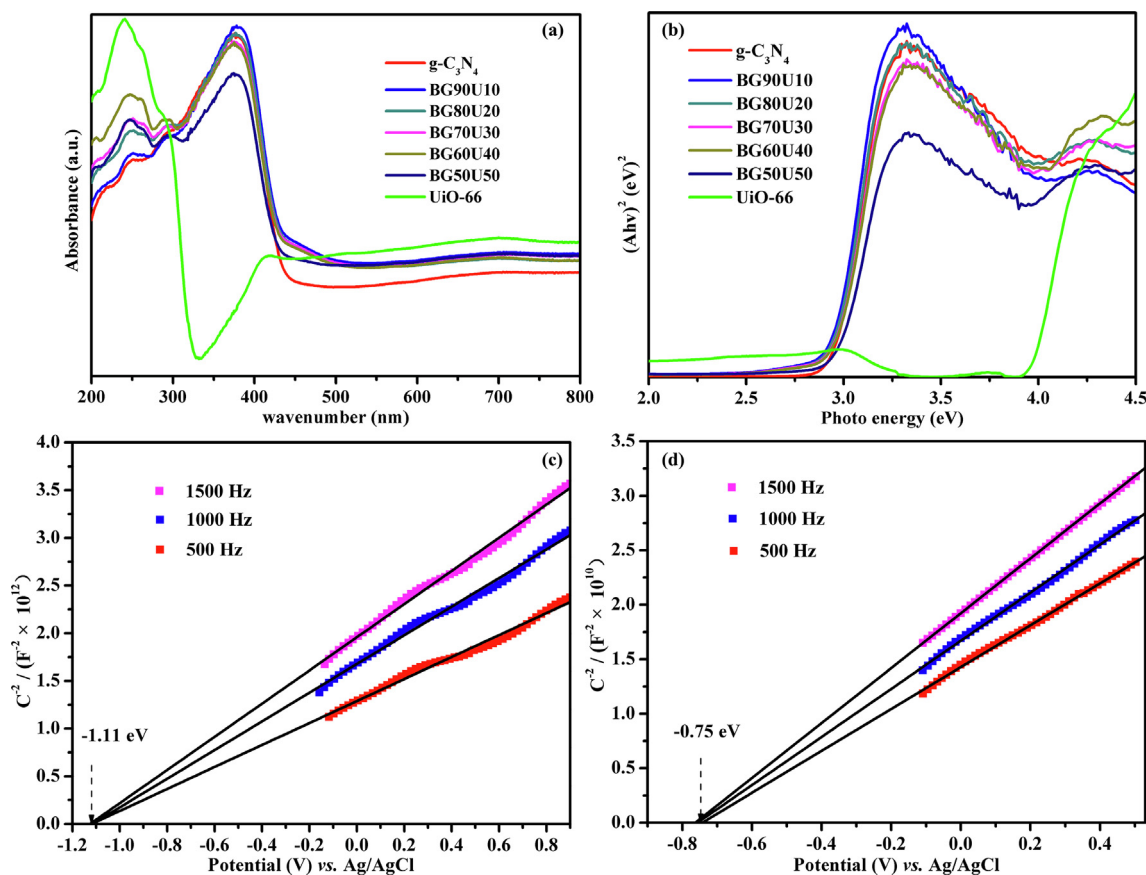
Fig. 7. (a) The UV–Vis DRS and (b) E_g plots of the g-C$_3$N$_4$, UiO-66, series composites. Mott-Schottky curves of (c) g-C$_3$N$_4$ and (d) UiO-66 at different frequencies.
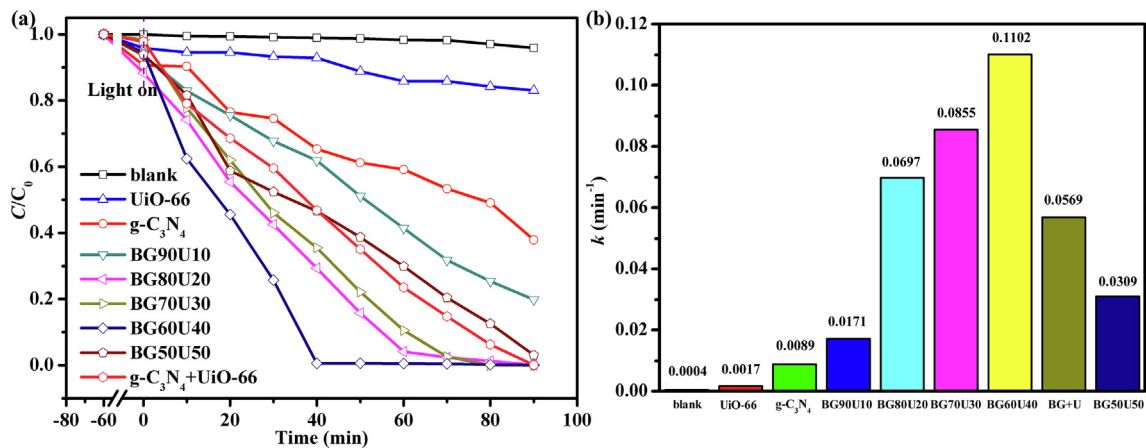

Fig. 8. (a) The photocatalytic Cr(VI) reduction over the samples under white light irradiation. (b) The photocatalytic Cr(VI) reduction rates (k values) over the different photocatalysts.

Table 1
Comparison of the photocatalytic Cr(VI) reduction activities of some counterpart photocatalysts.

| Photocatalyst/Amount (mg)	V (mL)/C_0 (mg L^{-1})/pH	Light source	T (min)	1st cycle efficiency (%)	Ref.
UiO-66(NH$_2$)/20	40/10/2.0	300 W Xe lamp	80	97	[55]
g-C$_3$N$_4$/MIL-53(Fe)/20	50/10/2.0–3.0	500 W Xe lamp (> 420 nm)	180	99	[28]
g-C$_3$N$_4$/NH$_2$-MIL-101(Fe)/20	40/10/2.0	300 W Xe lamp (> 400 nm)	60	100	[60]
g-C$_3$N$_4$/MIL-100(Fe)/100	200/10/2.0	300 W Xe lamp	80	97	[34]
g-C$_3$N$_4$/TiO$_2$/20	20/5.2/3.0	300 W Xe lamp (> 400 nm)	300	96	[61]
g-C$_3$N$_4$/ZnO/50	25/6.5/7.0	500 W Xe lamp (> 400 nm)	100	78	[62]
g-C$_3$N$_4$/Bi$_{12}$GeO$_{20}$/300	100/10/2.5	300 W Dy lamp (> 400 nm)	180	100	[63]
g-C$_3$N$_4$/GO/BiFeO$_3$/500	200/5/2.0	300 W Xe lamp (> 400 nm)	90	100	[64]
g-C$_3$N$_4$/UiO-66/100	200/10/2.0	300 W Xe lamp	40	99	This work
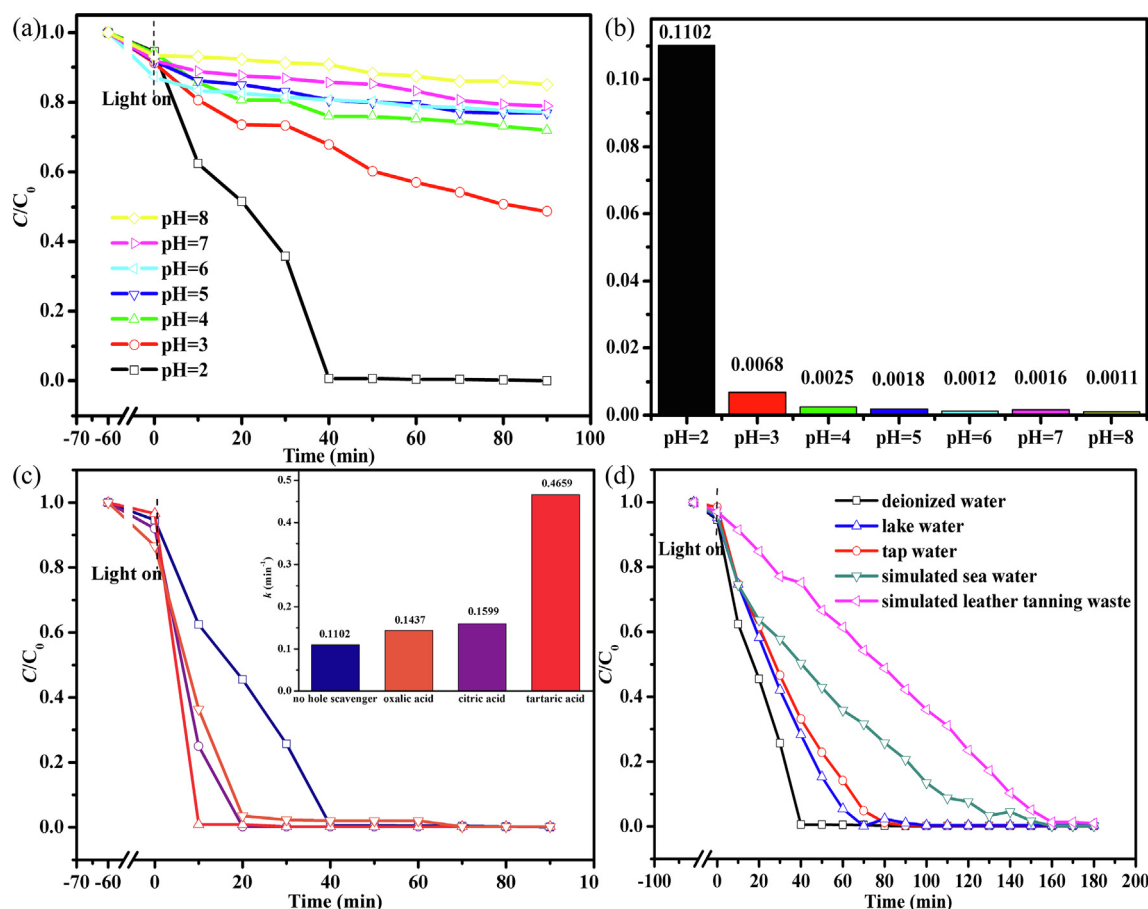
Fig. 9. (a) The effect of initial pH on Cr(VI) reduction. (b) The *k* values over the different of initial pH photocatalysts. (c) Photo-reduction of Cr(VI) with different hole scavenger. (d) The effect of different water quality on the photocatalytic Cr(VI) reduction. Conditions: BG60U40 = 100 mg, Cr(VI) = 10 mg L^{-1} (lake/tap/simulated sea water) or 30 mg L^{-1} (simulated leather tanning waste water), 200 mL, pH = 2.0.

electron and hole charge would be accelerated and the Cr(VI) reduction would be enhanced. To test the influence of some organics toward Cr (VI) reduction, some organics like citric acid, tartaric acid and oxalic acid were chosen as hole scavengers to conduct series experiments at pH = 2.0. As illustrated in Fig. 9c, the introduction of selected hole scavengers can increase photocatalytic Cr(VI) reduction activity, following the order of tartaric acid (two α-hydroxyl groups) > citric acid (one α-hydroxyl groups) > oxalic acid (zero α-hydroxyl groups), which was comparable to the previous reports [34,69,70]. The consumption of holes via the addition of organics will lead to more electrons being escaped to reduce Cr(VI), further increasing the Cr(VI) reduction efficiency and reaction rate.

3.2.4. Photocatalytic Cr(VI) reduction performances in different simulated wastewater samples

To investigate the influence of co-existing ions and the possibility of practical applications, different aqueous Cr(VI) solutions formulated by tap water, lake water, and simulated sea water, simulated leather tanning water were tested over BG60U40 under white light. The parameters of water quality are shown in the Table S2 [71,72]. The results revealed that the Cr(VI) reduction performances were inhibited in simulated wastewater formulated with tap and lake water (Fig. 9d). It was found that the Cr(VI) reduction efficiencies and reaction rates in lake water was superior to those in tap water solution, indicating that the dissolved organic matter (DOM, which was generally quantified by both TOC and UV$_{254}$, and listed in Table S3) in the lake water can deplete the photoinduced holes to accelerate the separation of photo-induced electron-hole pairs. Also, the photocatalytic activities of BG60U40 in simulated sea water and leather tanning waste water were

obviously weakened, in which the hexavalent chromium was reduced completely up to 160 min (Fig. 9d). It may be due to the inhibition of photocatalysis by high concentration of foreign ions in simulated sea water and simulated leather tanning waste water [71].

3.2.5. Reusability and stability of BG60U40

To further valuate the practical application potential of BG60U40 photocatalyst, six runs' photocatalytic reduction experiments were carried out. As depicted in Fig. 10a, the photocatalytic Cr(VI) reduction performance of BG60U40 displayed no obvious decline after six runs' usage, implying that BG60U40 photocatalyst was stable and highly efficient during long-term operation. The stability of BG60U40 was further confirmed by the nearly identical PXRD patterns (Fig. 10b), SEM and TEM (Fig. S3). As shown in Fig. 10b, the major XRD peaks remained, but the peak width is wider than that before photocatalysis, indicating that the structure of the composites was slightly affected. However, it was observed from the SEM and TEM images that no noticeable changes were happened to the morphologies of BG60U40 (Fig. S3).

3.2.6. The mechanism of photocatalytic Cr(VI) reduction over BG60U40

Photoluminescence (PL) spectroscopy and electrochemical impedance spectroscopy (EIS) measurements were introduced to elucidate the effect of g-C$_3$N$_4$ coating and its interfacial contact with UiO-66 on photocatalytic reduction mechanism. The higher photoluminescence signal implied the higher recombination rate of photoinduced electrons and holes [73]. In the PL spectrum of pristine g-C$_3$N$_4$, a strong emission peak could be observed at ca. 440 nm. However, the emission peak quenching at 440 nm occurs over BG60U40 (Fig. 11a), indicating that
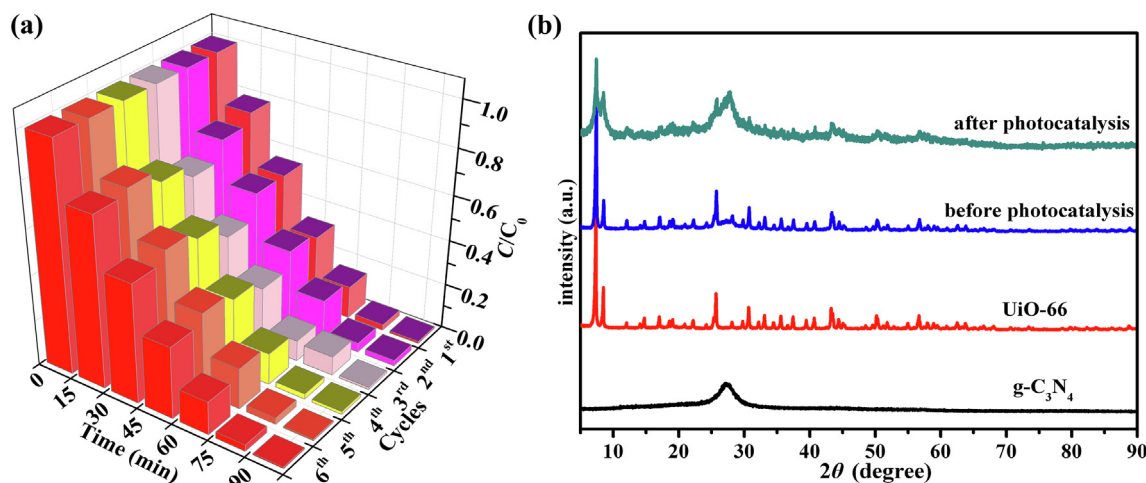
Fig. 10. (a) The cyclic experiments of photocatalytic Cr(VI) reaction over BG60U40. (b) PXRD patterns of BG60U40 before and after 6th cyclic experiments.

BG60U40 can maintain the longer lifetime of photo-induced charge carriers than g-C_3N_4. The EIS measurements as illustrated in Fig. 11b further clarified the charge-transfer effect of series BGxUy composites and the individual components. It was clear to find the diameter of arc radius followed in the order of g-C_3N_4 > BG70U30 > BG50U50 > BG90U10 > UiO-66 > BG80U20 > BG60U40, confirming that 2D/3D BG60U40 heterojunction shows better charge carrier separation and interfacial charge transfer than the pristine g-C_3N_4, UiO-66, and other composites with different ratio. The equivalent circuit (inset of Fig. 11b) is obtained to fit the electrochemical impedance spectra, in which Rs, Rct and CPE are the solution resistance, the charge transfer between the electrode and the electrolyte along with the constant phase element, respectively [74]. The Rct value of BG60U40 (105 Ω) is significantly lower than those of g-C_3N_4 (502 Ω) and UiO-66 (340 Ω) (Table S4), which indicates that BG60U40 can improve the separation and transmission efficiency of photogenerated electron-hole pairs [75].

In order to ascertain the primary active species in the Cr(VI) reduction process over BG60U40 and to get insight into the corresponding reaction mechanism, the ESR measurements were conducted to determine the formed active species over the BG60U40, g-C_3N_4 and UiO-66 (Fig. 11c–f). The characteristic ESR signals of both·O_2^- and ·OH with intensity 1:1:1:1 and 1:2:2:1 are detected over BG60U40 upon white light irradiation; however, no signal is detected in the dark condition. As well, the corresponding signal intensities at 10 min's illumination are stronger than those at 5 min, which confirms that both ·O_2^- and ·OH are produced in the photocatalytic process. It was also worthy to noting that ·OH signals are observed over UiO-66 upon the white irradiation (Fig. 11f), but ·OH signals can't be detected over pristine g-C_3N_4 under the identical conditions (Fig. 11e). Considering that the position of the valence band (VB, 1.89 eV *vs* NHE) of g-C_3N_4 is higher than the standard potential (2.40 eV *vs* NHE) of the OH$^-$/·OH pair (Fig. 12d), the photogenerated holes on the surface of g-C_3N_4 cannot react with OH$^-$/H_2O to form ·OH. On the other hand, the position of HOMO (3.35 eV *vs* NHE) of UiO-66 is lower than that of OH$^-$/·OH pairs (2.40 eV *vs* NHE), which may oxidize OH$^-$ or H_2O to form ·OH [26].

The high charge utilization efficiency in the BG60U40 heterostructure drives us to further study the interactions between the g-C_3N_4 and UiO-66 by density functional theory (DFT) calculations. The most stable structure of monolayer g-C_3N_4 on UiO-66 surface as shown in Fig. 12a, and the chemical interaction can also be affirmed by the electron density difference as depicted in Fig. 12b. The differential charge density calculation indicates that the electron density around C atoms (blue) on UiO-66 surface decreased, while the electron density around C and N atoms (yellow) of monolayer g-C_3N_4 increased after the formation of BG60U40 heterostructure. The Bader charge analysis is carried out to evaluate the charge transfer within BG60U40, in which the atom numbers in the Bader charge analysis are illustrated in Fig. S4, Tables S5 and S6, respectively. It was found that the positive charge of carbon atoms on the surface of UiO-66 increased significantly, especially at the position bonded with three N atoms from g-C_3N_4, indicating that the electrons over the surface of UiO-66 are transferred to g-C_3N_4 within BG60U40. In all, the DFT calculation results are in accordance with the above experimental results.

In all, the Z-scheme mechanism of photocatalytic Cr(VI) reduction over g-C_3N_4/UiO-66 is proposed as illustrated in Fig. 12d. And, the active species in the photocatalytic reaction system, both pure materials can produce photo-induced electrons and holes excited by white light. The photo-generated holes tend to be remained in the HOMO of UiO-66, meanwhile, the photogenerated electrons can be transferred from the UiO-66's LUMO to the g-C_3N_4's CB. Thus, the separation of photogenerated e$^-$ and h$^+$ can be promoted. To study the roles of active species in the photocatalytic Cr(VI) reduction over BG60U40, series capture experiments toward active species were designed and conducted (Fig. 12c). In detail, isopropyl alcohol (IPA, 0.2 mmol L^{-1}), EDTA-2Na (0.2 mmol L^{-1}) and AgNO$_3$ (0.2 mmol L^{-1}) were introduced to capture ·OH radicals, h$^+$ and e$^-$ [76,77], respectively. As well, nitrogen gas is introduced in the experiment to remove dissolved oxygen gas in reaction solution to avoid the formation of ·O_2^- [78]. The efficiency of Cr(VI) reduction was decreased obviously when the e$^-$ of the system has been trapped, which demonstrated that hexavalent chromium is reduced to trivalent chromium by electrons over the surface of g-C_3N_4 via sequential one-electron-transfer steps (Eq. (5)) [78,79]. And ·O_2^- is considered to be a mediator for reducing Cr(VI) [64,80,81] via Eq. (6) [78], which can be generated as the CB value of g-C_3N_4 is -0.91 eV *vs*. NHE, much more negative than the potential of O_2/·O_2^- (-0.33 eV *vs*. NHE). It had been reported that ·O_2^- react with Cr(VI) to generate Cr(V) (Eq. (7)) [82], so that the Cr(VI) reduction efficiency over BG60U40 decreased obviously in the N_2 atmosphere in this work, implying that ·O_2^- is the active specie to reduce Cr(VI). And, the Cr(VI) reduction efficiency decreased when ·OH has been trapped by IPA, which was assigned to the equilibrium shifting toward Cr(VI) as listed Eqs (6), (8) and (9) [78,82]. When the active species of h$^+$ in the photocatalytic reaction was trapped, the Cr(VI) reduction efficiency is improved significantly, indicating that H_2O or OH$^-$ have been oxidized by h$^+$ to generated the active species ·OH (Eq. (10)) [78]. The ·OH formation will mainly facilitate the separation of electrons and holes to further promote the Cr(VI) reduction activity, and might exert minor effect on the oxidation from Cr(V) back to Cr(VI) as displayed in Eq. (11) [79]. As illustrated in Fig. 12c, the Cr(VI) reduction activity of BG60U40 was significantly restrained in the presence of AgNO$_3$,
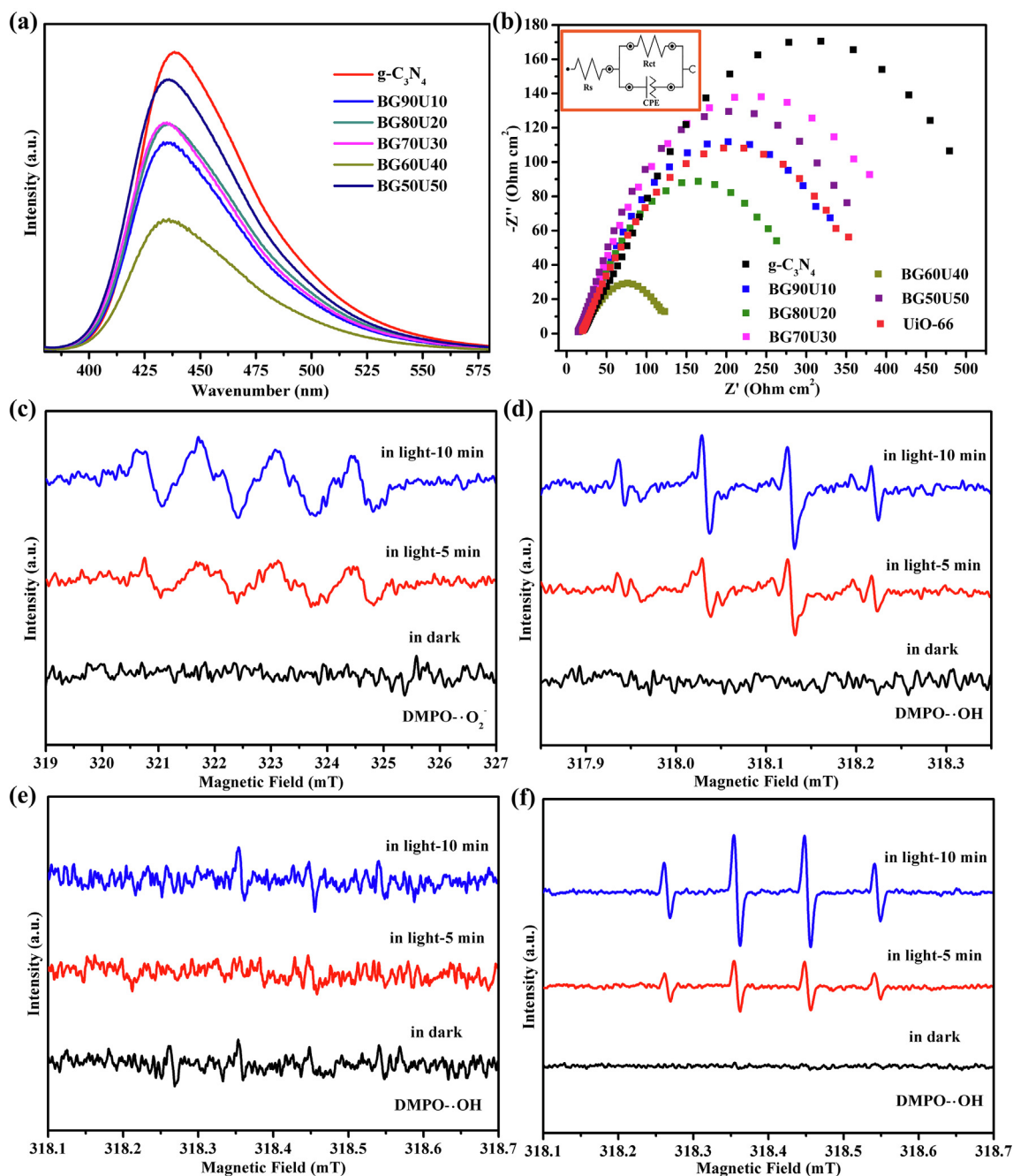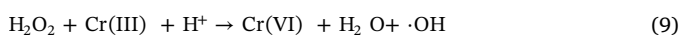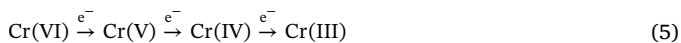
Fig. 11. The PL spectra (a), EIS analysis and equivalent circuit (inset) of the samples (b), the ESR spectra of active species trapped by DMPO in aqueous dispersion for $\cdot O_2^-$ over BG60U40 (c) along with $\cdot OH$ over (d) BG60U40, (e) g-C$_3$N$_4$, (f) UiO-66.

implying that e^- was the major active species. The improved Cr(VI) reduction behavior was due to that the Z-scheme heterostructures could facilitate to effectively separate photoinduced electron-hole pairs, as well to improve the redox capacity of photocatalysts with the aid of the increase in redox potential [83].

$$Cr(VI) \xrightarrow{e^-} Cr(V) \xrightarrow{e^-} Cr(IV) \xrightarrow{e^-} Cr(III) \tag{5}$$

$$O_2 + e^- \rightarrow \cdot O_2^- \tag{6}$$

$$\cdot O_2^- + Cr(VI) \rightarrow Cr(V) + O_2 \tag{7}$$

$$2 \cdot O_2^- + 2H^+ \rightarrow H_2O_2 + O_2 \tag{8}$$

$$H_2O_2 + Cr(III) + H^+ \rightarrow Cr(VI) + H_2O + \cdot OH \tag{9}$$

$$2H_2O + h^+ \rightarrow 2 \cdot OH + H^+ \tag{10}$$

$$Cr(V) + h^+/\cdot OH \rightarrow Cr(VI) + OH^- \tag{11}$$

4. Conclusions

The facile construction of series 2D/3D g-C$_3$N$_4$/UiO-66 (BGxUy) composites was achieved, in which the optimal BG60U40 composite photocatalyst displayed superior Cr(VI) reduction performance than pristine g-C$_3$N$_4$ and UiO-66 upon the illumination of white light. The experiment results of electro-chemical and PL measurements showed that the improved photocatalytic reaction was assigned to the enhanced charge transfer over the interface of Z-scheme heterostructure. As well, the influences of pH and hole scavengers on photocatalytic Cr(VI)
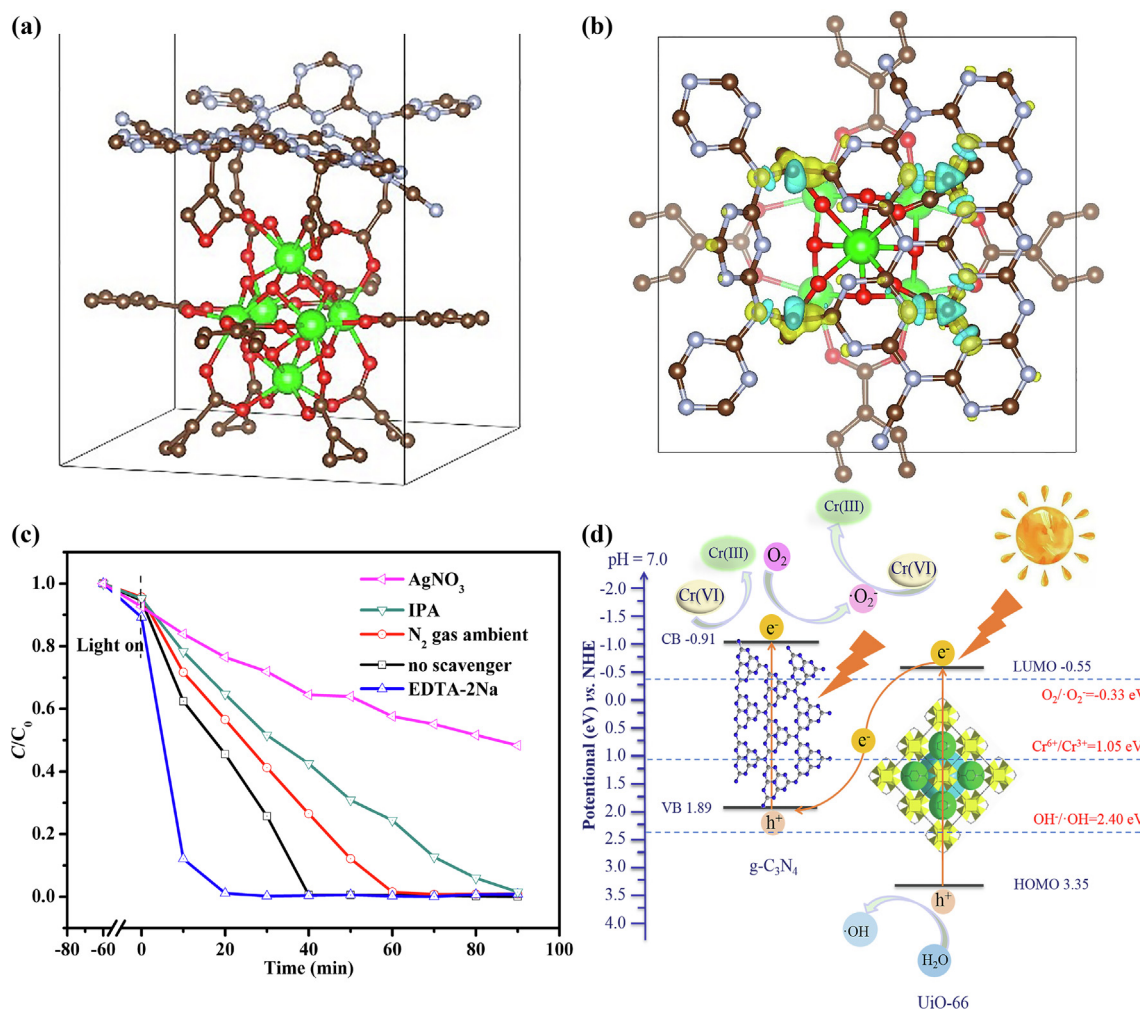
Fig. 12. (a) The most stable structure of g-C$_3$N$_4$ on UiO-66 surface after geometry relaxation. The green, brown, light blue sphere represents Zr, C and N atom, respectively. (b) Electron density difference around UiO-66 surface and g-C$_3$N$_4$ fragment when g-C$_3$N$_4$ wrapped on the UiO-66 surface from the top view. The yellow area represents increasing of electron density, blue area indicates decline of electron density.(c) Effects of different scavengers on Cr(VI) reduction in the presence of BG60U40. (d) A simplified diagram of photocatalytic Cr(VI) reduction mechanism of g-C$_3$N$_4$/UiO-66. (For interpretation of the references to colour in this figure legend, the reader is referred to the web version of this article.)

reduction were tested. It was worthy to noting that Cr(VI) reduction was also accomplished for simulated wastewater prepared with tap water and lake water, simulated sea water (high salinity wastewater) and simulated leather tanning wastewater. The ESR determination, series caputure experiments and DFT calculations clarified the corresponding Cr(VI) reduction mechanism. Finally, the cycling tests exhibited that the BG60U40 composite was stable and recyclable. This work further tested the combination of MOFs and g-C$_3$N$_4$ was a prospective strategy for enhancing the photocatalytic performance.

Conflict of interest

None.

Appendix A. Supplementary data

Supplementary data to this article can be found online at https://doi.org/10.1016/j.cej.2019.121944.

References

[1] J.H. Cavka, S. Jakobsen, U. Olsbye, N. Guillou, C. Lamberti, S. Bordiga, K.P. Lillerud, A new zirconium inorganic building brick forming metal organic frameworks with exceptional stability, J. Am. Chem. Soc. 130 (2008) 13850–13851.

[2] H. Wu, T. Yildirim, W. Zhou, Exceptional mechanical stability of highly porous zirconium metal-organic framework UiO-66 and its important implications, J. Phys. Chem. Lett. 4 (2013) 925–930.

[3] A.D. Wiersum, E. Soubeyrand-Lenoir, Q. Yang, B. Moulin, V. Guillerm, M.B. Yahia, S. Bourrelly, A. Vimont, S. Miller, C. Vagner, M. Daturi, G. Clet, C. Serre, G. Maurin, P.L. Llewellyn, An evaluation of UiO-66 for gas-based applications, Chem. -Asian J. 6 (2011) 3270–3280.

[4] L. Valenzano, B. Civalleri, S. Chavan, S. Bordiga, M.H. Nilsen, S. Jakobsen, K.P. Lillerud, C. Lamberti, Disclosing the complex structure of UiO-66 metal organic framework: A synergic combination of experiment and theory, Chem. Mater. 23 (2011) 1700–1718.

[5] W. Fu-Xue, W. Chong-Chen, W. Peng, X. Bi-Cong, Syntheses and applications of UiO series of MOFs, Chin. J. Inorg. Chem. 33 (2017) 713–737.

[6] S.-N. Kim, Y.-R. Lee, S.-H. Hong, M.-S. Jang, W.-S. Ahn, Pilot-scale synthesis of a zirconium-benzenedicarboxylate UiO-66 for CO$_2$ adsorption and catalysis, Catal. Today 245 (2015) 54–60.

[7] F. Vermoortele, B. Bueken, G. Le Bars, B. Van de Voorde, M. Vandichel,

K. Houthoofd, A. Vimont, M. Daturi, M. Waroquier, V. Van Speybroeck, C. Kirschhock, D.E. De Vos, Synthesis modulation as a tool to increase the catalytic activity of metal-organic frameworks: The unique case of UiO-66(Zr), J. Am. Chem. Soc. 135 (2013) 11465–11468.

[8] S. Chavan, J.G. Vitillo, D. Gianolio, O. Zavorotynska, B. Civalleri, S. Jakobsen, M.H. Nilsen, L. Valenzano, C. Lamberti, K.P. Lillerud, S. Bordiga, H₂ storage in isostructural UiO-67 and UiO-66 MOFs, Phys. Chem. Chem. Phys. 14 (2012) 1614–1626.

[9] H.R. Abid, H. Tian, H.-M. Ang, M.O. Tade, C.E. Buckley, S. Wang, Nanosize Zr-metal organic framework (UiO-66) for hydrogen and carbon dioxide storage, Chem. Eng. J. 187 (2012) 415–420.

[10] Q. Yang, V. Guillerm, F. Ragon, A.D. Wiersum, P.L. Llewellyn, C. Zhong, T. Devic, C. Serre, G. Maurin, CH₄ storage and CO₂ capture in highly porous zirconium oxide based metal-organic frameworks, Chem. Commun. 48 (2012) 9831–9833.

[11] N. Chang, X.-P. Yan, Exploring reverse shape selectivity and molecular sieving effect of metal-organic framework UiO-66 coated capillary column for gas chromatographic separation, J. Chromatogr. A 1257 (2012) 116–124.

[12] D. Sun, Y. Fu, W. Liu, L. Ye, D. Wang, L. Yang, X. Fu, Z. Li, Studies on photocatalytic CO₂ reduction over NH₂-UiO-66(Zr) and its derivatives: Towards a better understanding of photocatalysis on metal-organic frameworks, Chem. -Eur. J. 19 (2013) 14279–14285.

[13] L. Shen, W. Wu, R. Liang, R. Lin, L. Wu, Highly dispersed palladium nanoparticles anchored on UiO-66(NH₂) metal-organic framework as a reusable and dual functional visible-light-driven photocatalyst, Nanoscale 5 (2013) 9374–9382.

[14] C. Gomes Silva, I. Luz, F.X. Llabrés i Xamena, A. Corma, H. García, Water stable Zr-benzenedicarboxylate metal-organic frameworks as photocatalysts for hydrogen generation, Chem. -Eur. J. 16 (2010) 11133–11138.

[15] J. Long, S. Wang, Z. Ding, S. Wang, Y. Zhou, L. Huang, X. Wang, Amine-functionalized zirconium metal-organic framework as efficient visible-light photocatalyst for aerobic organic transformations, Chem. Commun. 48 (2012) 11656–11658.

[16] L. Shen, S. Liang, W. Wu, R. Liang, L. Wu, CdS-decorated UiO-66(NH₂) nanocomposites fabricated by a facile photodeposition process: an efficient and stable visible-light-driven photocatalyst for selective oxidation of alcohols, J. Mate. Chem. A 1 (2013) 11473–11482.

[17] D. Sun, Z. Li, Robust Ti- and Zr-based metal-organic frameworks for photocatalysis, Chin. J. Chem. 35 (2017) 135–147.

[18] G. Zhou, M.-F. Wu, Q.-J. Xing, F. Li, H. Liu, X.-B. Luo, J.-P. Zou, J.-M. Luo, A.-Q. Zhang, Synthesis and characterizations of metal-free Semiconductor/MOFs with good stability and high photocatalytic activity for H₂ evolution: a novel Z-Scheme heterostructured photocatalyst formed by covalent bonds, Appl. Catal. B: Environ. 220 (2018) 607–614.

[19] Y.S. Seo, N.A. Khan, S.H. Jhung, Adsorptive removal of methyl-chlorophenoxypropionic acid from water with a metal-organic framework, Chem. Eng. J. 270 (2015) 22–27.

[20] M.A. Nasalevich, C.H. Hendon, J.G. Santaclara, K. Svane, B. van der Linden, S.L. Veber, M.V. Fedin, A.J. Houtepen, M.A. van der Veen, F. Kapteijn, A. Walsh, J. Gascon, Electronic origins of photocatalytic activity in d⁰ metal organic frameworks, Sci. Rep. 6 (2016) 23676.

[21] A. Santiago Portillo, H.G. Baldoví, M.T. García Fernandez, S. Navalón, P. Atienzar, B. Ferrer, M. Alvaro, H. Garcia, Z. Li, Ti as mediator in the photoinduced electron transfer of mixed-metal NH₂-UiO- 66(Zr/Ti): Transient absorption spectroscopy study and application in photovoltaic cell, J. Phys. Chem. C 121 (2017) 7015–7024.

[22] J. Zhang, N. Gao, F. Chen, T. Zhang, G. Zhang, D. Wang, X. Xie, D. Cai, X. Ma, L. Wu, Z. Wu, Improvement of Cr(VI) photoreduction under visible-light by g-C₃N₄ modified by nano-network structured palygorskite, Chem. Eng. J. 358 (2019) 398–407.

[23] C.-C. Wang, X.-H. Yi, P. Wang, Powerful combination of MOFs and C₃N₄ for enhanced photocatalytic performance, Appl. Catal. B: Environ. 247 (2019) 24–48.

[24] R. Wang, L. Gu, J. Zhou, X. Liu, F. Teng, C. Li, Y. Shen, Y. Yuan, Quasi-polymeric metal-organic framework UiO-66/g-C₃N₄ heterojunctions for enhanced photocatalytic hydrogen evolution under visible light irradiation, Adv. Mater. Interfaces 2 (2015) 1500037.

[25] X. Zhang, Y. Yang, W. Huang, Y. Yang, Y. Wang, C. He, N. Liu, M. Wu, L. Tang, g-C₃N₄/UiO-66 nanohybrids with enhanced photocatalytic activities for the oxidation of dye under visible light irradiation, Mater. Res. Bull. 99 (2018) 349–358.

[26] Y. Zhang, J. Zhou, Q. Feng, X. Chen, Z. Hu, Visible light photocatalytic degradation of MB using UiO-66/g-C₃N₄ heterojunction nanocatalyst, Chemosphere 212 (2018) 523–532.

[27] L. Shi, T. Wang, H. Zhang, K. Chang, J. Ye, Electrostatic self-assembly of nanosized carbon nitride nanosheet onto a zirconium metal-organic framework for enhanced photocatalytic CO₂ reduction, Adv. Funct. Mater. 25 (2015) 5360–5367.

[28] W. Huang, N. Liu, X. Zhang, M. Wu, L. Tang, Metal organic framework g-C₃N₄/MIL-53(Fe) heterojunctions with enhanced photocatalytic activity for Cr(VI) reduction under visible light, Appl. Surf. Sci. 425 (2017) 107–116.

[29] J.J. Testa, M.A. Grela, M.I. Litter, Heterogeneous photocatalytic reduction of chromium(VI) over TiO₂ particles in the presence of oxalate: Involvement of Cr(V) species, Environ. Sci. Technol. 38 (2004) 1589–1594.

[30] C.-C. Wang, X.-D. Du, J. Li, X.-X. Guo, P. Wang, J. Zhang, Photocatalytic Cr(VI) reduction in metal-organic frameworks: A mini-review, Appl. Catal. B: Environ. 193 (2016) 198–216.

[31] G. Chen, J. Han, Y. Mu, H. Yu, L. Qin, Two-stage chromium isotope fractionation during microbial Cr(VI) reduction, Water Res. 148 (2019) 10–18.

[32] R. Liang, F. Jing, L. Shen, N. Qin, L. Wu, MIL-53(Fe) as a highly efficient bifunctional photocatalyst for the simultaneous reduction of Cr(VI) and oxidation of dyes, J. Hazard. Mater. 287 (2015) 364–372.

[33] S.-H. Zhang, M.-F. Wu, T.-T. Tang, Q.-J. Xing, C.-Q. Peng, F. Li, H. Liu, X.-B. Luo, J.-P. Zou, X.-B. Min, J.-M. Luo, Mechanism investigation of anoxic Cr(VI) removal by nano zero-valent iron based on XPS analysis in time scale, Chem. Eng. J. 335 (2018) 945–953.

[34] X.-H. Yi, F.-X. Wang, X.-D. Du, P. Wang, C.-C. Wang, Facile fabrication of BUC-21/g-C₃N₄ composites and their enhanced photocatalytic Cr(VI) reduction performances under simulated sunlight, Appl. Organomet. Chemi. 33 (2019) e4621.

[35] C. Athanasekou, G.E. Romanos, S.K. Papageorgiou, G.K. Manolis, F. Katsaros, P. Falaras, Photocatalytic degradation of hexavalent chromium emerging contaminant via advanced titanium dioxide nanostructures, Chem. Eng. J. 318 (2017) 171–180.

[36] H. Yu, R. Shi, Y. Zhao, T. Bian, Y. Zhao, C. Zhou, W. Gin, L.Z. Wu, C.H. Tung, T. Zhang, Alkali-assisted synthesis of nitrogen deficient graphitic carbon nitride with tunable band structures for efficient visible-light-driven hydrogen evolution, Adv. Mater. 29 (2017) 1605148–1605154.

[37] A. Ghorbanpour, L.D. Huelsenbeck, D.-M. Smilgies, G. Giri, Oriented UiO-66 thin films through solution shearing, CrystEngComm 20 (2018) 294–300.

[38] Y. Chen, X. Wang, Template-free synthesis of hollow g-C₃N₄ polymer with vesicle structure for enhanced photocatalytic water splitting, J. Phys. Chem. C 122 (2018) 3786–3793.

[39] G. Li, X. Nie, J. Chen, Q. Jiang, T. An, P.K. Wong, H. Zhang, H. Zhao, H. Yamashita, Enhanced visible-light-driven photocatalytic inactivation of Escherichia coli using g-C₃N₄/TiO₂ hybrid photocatalyst synthesized using a hydrothermal-calcination approach, Water Res. 86 (2015) 17–24.

[40] L. Ye, J. Liu, Z. Jiang, T. Peng, L. Zan, Facets coupling of BiOBr-g-C₃N₄ composite photocatalyst for enhanced visible-light-driven photocatalytic activity, Appl. Catal. B: Environ. 142–143 (2013) 1–7.

[41] J. Yang, Y. Dai, X. Zhu, Z. Wang, Y. Li, Q. Zhuang, J. Shi, J. Gu, Metal-organic frameworks with inherent recognition sites for selective phosphate sensing through their coordination-induced fluorescence enhancement effect, J. Mate. Chem. A 3 (2015) 7445–7452.

[42] X.-Y. Xu, C. Chu, H. Fu, X.-D. Du, P. Wang, W. Zheng, C.-C. Wang, Light-responsive UiO-66-NH₂/Ag₃PO₄ MOF-nanoparticle composites for the capture and release of sulfamethoxazole, Chem. Eng. J. 350 (2018) 436–444.

[43] W. Xiong, Z. Zeng, X. Li, G. Zeng, R. Xiao, Z. Yang, Y. Zhou, C. Zhang, M. Cheng, L. Hu, C. Zhou, L. Qin, R. Xu, Y. Zhang, Multi-walled carbon nanotube/amino-functionalized MIL-53(Fe) composites: Remarkable adsorptive removal of antibiotics from aqueous solutions, Chemosphere 210 (2018) 1061–1069.

[44] J. Ran, B. Zhu, S.-Z. Qiao, Phosphorene Co-catalyst advancing highly efficient visible-light photocatalytic hydrogen production, Angew. Chem. Int. Ed. 56 (2017) 10373–10377.

[45] H. Dong, X. Guo, C. Yang, Z. Ouyang, Synthesis of g-C₃N₄ by different precursors under burning explosion effect and its photocatalytic degradation for tylosin, Appl. Catal. B: Environ. 230 (2018) 65–76.

[46] J. Yu, C. Wang, W. Yuan, Y. Shen, A. Xie, B, N Co-doped three dimensional carbon aerogels with excellent electrochemical performance for the oxygen reduction reaction, Chem. -Eur. J. 25 (2019) 2877–2883.

[47] K. Dai, J. Lv, J. Zhang, C. Liang, G. Zhu, Band structure engineering design of g-C₃N₄/ZnS/SnS₂ ternary heterojunction visible-light photocatalyst with ZnS as electron transport buffer material, J. Alloys Compd. 778 (2019) 215–223.

[48] F. Dong, L. Wu, Y. Sun, M. Fu, Z. Wu, S.C. Lee, Efficient synthesis of polymeric g-C₃N₄ layered materials as novel efficient visible light driven photocatalysts, J. Mate. Chem. 21 (2011) 15171–15174.

[49] J. Chen, Z. Mao, L. Zhang, Y. Tang, D. Wang, L. Bie, B.D. Fahlman, Direct production of nitrogen-doped porous carbon from urea via magnesiothermic reduction, Carbon 130 (2018) 41–47.

[50] J. Barrio, A. Grafmüller, J. Tzadikov, M. Shalom, Halogen-hydrogen bonds: A general synthetic approach for highly photoactive carbon nitride with tunable properties, Appl. Catal. B: Environ. 237 (2018) 681–688.

[51] J. Ran, X. Wang, B. Zhu, S.-Z. Qiao, Strongly interactive 0D/2D hetero-structure of a ZnₓCd₁ ₋ ₓS nano-particle decorated phosphorene nano-sheet for enhanced visible-light photocatalytic H₂ production, Chem. Commun. 53 (2017) 9882–9885.

[52] H. Jia, W. He, B. Zhang, L. Yao, X. Yang, Z. Zheng, Facile synthesis of bismuth oxyhalide nanosheet films with distinct conduction type and photo-induced charge carrier behavior, Appl. Surf. Sci. 441 (2018) 832–840.

[53] Y. Pan, D. Li, H.-L. Jiang, Sodium-doped C₃N₄/MOF heterojunction composites with tunable band structures for photocatalysis: Interplay between light harvesting and electron transfer, Chem. -Eur. J. 24 (2018) 18403–18407.

[54] H. Wang, X. Yuan, Y. Wu, G. Zeng, X. Chen, L. Leng, H. Li, Synthesis and applications of novel graphitic carbon nitride/metal-organic frameworks mesoporous photocatalyst for dyes removal, Appl. Catal. B: Environ. 174–175 (2015) 445–454.

[55] L. Shen, R. Liang, M. Luo, F. Jing, L. Wu, Electronic effects of ligand substitution on metal-organic framework photocatalysts: the case study of UiO-66, Phys. Chem. Chem. Phys. 17 (2015) 117–121.

[56] J.-P. Zou, D.-D. Wu, J. Luo, Q.-J. Xing, X.-B. Luo, W.-H. Dong, S.-L. Luo, H.-M. Du, S.L. Suib, A strategy for one-pot conversion of organic pollutants into useful hydrocarbons through coupling photodegradation of MB with photoreduction of CO₂, ACS Catal. 6 (2016) 6861–6867.

[57] Y. Zhang, F. Zhang, Z. Yang, H. Xue, D.D. Dionysiou, Development of a new efficient visible-light-driven photocatalyst from SnS₂ and polyvinyl chloride, J. Catal. 344 (2016) 692–700.

[58] Q. Liang, J. Jin, C. Liu, S. Xu, C. Yao, Z. Li, Fabrication of the ternary heterojunction Cd₀.₅Zn₀.₅S@UIO-66@g-C₃N₄ for enhanced visible-light photocatalytic hydrogen evolution and degradation of organic pollutants, Inorg. Chem. Front. 5 (2018) 335–343.

[59] J. Liu, B. Cheng, J. Yu, A new understanding of the photocatalytic mechanism of the direct Z-scheme g-C₃N₄/TiO₂ heterostructure, Phys. Chem. Chem. Phys. 18 (2016)

31175–31183.

[60] B. Liu, Y. Wu, X. Han, J. Lv, J. Zhang, H. Shi, Facile synthesis of g-C3N4/amine-functionalized MIL-101(Fe) composites with efficient photocatalytic activities under visible light irradiation, J. Mater. Sci.: Mater. Electron. 29 (2018) 17591–17601.

[61] R. Mohini, N. Lakshminarasimhan, Coupled semiconductor nanocomposite g-C3N4/TiO2 with enhanced visible light photocatalytic activity, Mater. Res. Bull. 76 (2016) 370–375.

[62] W. Liu, M. Wang, C. Xu, S. Chen, Facile synthesis of g-C3N4/ZnO composite with enhanced visible light photooxidation and photoreduction properties, Chem. Eng. J. 209 (2012) 386–393.

[63] Z. Wan, G. Zhang, X. Wu, S. Yin, Novel visible-light-driven Z-scheme Bi12GeO20/g-C3N4 photocatalyst: Oxygen-induced pathway of organic pollutants degradation and proton assisted electron transfer mechanism of Cr(VI) reduction, Appl. Catal. B: Environ. 207 (2017) 17–26.

[64] X. Hu, W. Wang, G. Xie, H. Wang, X. Tan, Q. Jin, D. Zhou, Y. Zhao, Ternary assembly of g-C3N4/graphene oxide sheets/BiFeO3 heterojunction with enhanced photoreduction of Cr(VI) under visible-light irradiation, Chemosphere 216 (2019) 733–741.

[65] F.-X. Wang, X.-H. Yi, C.-C. Wang, J.-G. Deng, Photocatalytic Cr(VI) reduction and organic-pollutant degradation in a stable 2D coordination polymer, Chin. J. Catal. 38 (2017) 2141–2149.

[66] X.-D. Du, X.-H. Yi, P. Wang, W. Zheng, J. Deng, C.-C. Wang, Robust photocatalytic reduction of Cr(VI) on UiO-66-NH2(Zr/Hf) metal-organic framework membrane under sunlight irradiation, Chem. Eng. J. 356 (2019) 393–399.

[67] F. Zhang, Y. Zhang, C. Zhou, Z. Yang, H. Xue, D.D. Dionysiou, A new high efficiency visible-light photocatalyst made of SnS2 and conjugated derivative of polyvinyl alcohol and its application to Cr(VI) reduction, Chem. Eng. J. 324 (2017) 140–153.

[68] H. Wang, X. Yuan, Y. Wu, G. Zeng, X. Chen, L. Leng, Z. Wu, L. Jiang, H. Li, Facile synthesis of amino-functionalized titanium metal-organic frameworks and their superior visible-light photocatalytic activity for Cr(VI) reduction, J. Hazard. Mater. 286 (2015) 187–194.

[69] M. Rivero-Huguet, W.D. Marshall, Influence of various organic molecules on the reduction of hexavalent chromium mediated by zero-valent iron, Chemosphere 76 (2009) 1240–1248.

[70] C.E. Barrera-Díaz, V. Lugo-Lugo, B. Bilyeu, A review of chemical, electrochemical and biological methods for aqueous Cr(VI) reduction, J. Hazard. Mater. 223–224 (2012) 1–12.

[71] A. Albrbar, A. Bjelajac, V. Djokic, J. Miladinovic, D. Janackovic, R. Petrovic, Photocatalytic efficiency of titania photocatalysts in saline waters, J. Serb. Chem. Soc. 79 (2014) 1127–1140.

[72] X. Wang, S.O. Pehkonen, A.K. Ray, Removal of aqueous Cr(VI) by a combination of photocatalytic reduction and coprecipitation, Ind. Eng. Chem. Res. 43 (2004) 1665–1672.

[73] Y.-C. Nie, F. Yu, L.-C. Wang, Q.-J. Xing, X. Liu, Y. Pei, J.-P. Zou, W.-L. Dai, Y. Li, S.L. Suib, Photocatalytic degradation of organic pollutants coupled with simultaneous photocatalytic H2 evolution over graphene quantum dots/Mn-N-TiO2/g-C3N4 composite catalysts: Performance and mechanism, Appl. Catal. B: Environ. 227 (2018) 312–321.

[74] B. Xin, Z. Ren, P. Wang, J. Liu, L. Jing, H. Fu, Study on the mechanisms of photoinduced carriers separation and recombination for Fe3+-TiO2 photocatalysts, Appl. Surf. Sci. 253 (2007) 4390–4395.

[75] B. Song, T. Wang, H. Sun, Q. Shao, J. Zhao, K. Song, L. Hao, L. Wang, Z. Guo, Two-step hydrothermally synthesized carbon nanodots/WO3 photocatalysts with enhanced photocatalytic performance, Dalton Trans. 46 (2017) 15769–15777.

[76] W. Wu, J. Wang, T. Zhang, S. Jiang, X. Ma, G. Zhang, X. Zhang, X. Chen, B. Li, Controllable synthesis of Ag/AgCl@MIL-88A via in situ growth method for morphology-dependent photocatalytic performance, J. Mate. Chem. C 7 (2019) 5451–5460.

[77] Y. Tian, W. Li, C. Zhao, Y. Wang, B. Zhang, Q. Zhang, Fabrication of hollow mesoporous SiO2-BiOCl@PANI@Pd photocatalysts to improve the photocatalytic performance under visible light, Appl. Catal. B: Environ. 213 (2017) 136–146.

[78] J.-C. Wang, J. Ren, H.-C. Yao, L. Zhang, J.-S. Wang, S.-Q. Zang, L.-F. Han, Z.-J. Li, Synergistic photocatalysis of Cr(VI) reduction and 4-Chlorophenol degradation over hydroxylated α-Fe2O3 under visible light irradiation, J. Hazard. Mater. 311 (2016) 11–19.

[79] J.J. Testa, M.A. Grela, M.I. Litter, Experimental evidence in eavor of an initial one-electron-transfer process in the heterogeneous photocatalytic reduction of chromium(VI) over TiO2, Langmuir 17 (2001) 3515–3517.

[80] G. Dong, L. Zhang, Synthesis and enhanced Cr(VI) photoreduction property of formate anion containing graphitic carbon nitride, J. Phys. Chem. C 117 (2013) 4062–4068.

[81] F. Zhang, Y. Zhang, G. Zhang, Z. Yang, D.D. Dionysiou, A. Zhu, Exceptional synergistic enhancement of the photocatalytic activity of SnS2 by coupling with polyaniline and N-doped reduced graphene oxide, Appl. Catal. B: Environ. 236 (2018) 53–63.

[82] X. Hu, H. Ji, F. Chang, Y. Luo, Simultaneous photocatalytic Cr(VI) reduction and 2,4,6-TCP oxidation over g-C3N4 under visible light irradiation, Catal. Today 224 (2014) 34–40.

[83] J. Low, C. Jiang, B. Cheng, S. Wageh, A.A. Al-Ghamdi, J. Yu, A review of direct Z-scheme photocatalysts, Small Methods 1 (2017) 1700080.